Research Article

Nano Research
2024, 17(3): 1516–1524

ISSN 1998-0124 CN 11-5974/O4
https://doi.org/10.1007/s12274-023-5982-6

Cu nanowire array with designed interphases enabling high performance Si anode toward flexible lithium-ion battery

Pengfei Su[1], Ziqi Zhang[3], Linshan Luo[1], Zhiyong Zhang[1], Chaofei Lan[1], Yahui Li[1], Shaowen Xu[1], Shanpeng Pei[4], Guangyang Lin[1], Cheng Li[1], Xiang Han[2] (✉), Wei Huang[1] (✉), and Songyan Chen[1] (✉)

[1] *Fujian Provincial Key Laboratory of Semiconductors and Applications, Collaborative Innovation Center for Optoelectronic Semiconductors and Efficient Devices, Department of Physics, Xiamen University, Xiamen 361005, China*
[2] *College of Materials Science and Engineering, Nanjing Forestry University, Nanjing 210037, China*
[3] *Science and Technology on Analog Integrated Circuit Laboratory, Chongqing 400060, China*
[4] *Shandong Electric Power Engineering Consulting Institute Co., Ltd., Jinan 250013, China*

Received: 14 May 2023 / **Revised:** 26 June 2023 / **Accepted:** 3 July 2023

ABSTRACT

To meet the growing demand for wearable smart electronic devices, the development of flexible lithium-ion batteries (LIBs) is essential. Silicon is an ideal candidate for the anode material of flexible lithium-ion batteries due to its high specific capacity, low working potential, and earth abundance. The largest challenge in developing a flexible silicon anode is how to maintain structural integrity and ensure stable electrochemical reactions during external deformation. In this work, we propose a novel design for fabricating core–shell electrodes based on a copper nanowire (CuNW) array core and magnetron sputtered Si/C shell. The nanowire array structure has characteristics of bending under longitudinal stress and twisting under transverse stress, which helps to maintain the mechanical stability of the structure during electrode bending and cycling. The low-temperature annealing generates a small amount of Cu_3Si alloy, which enhances the connection strength between Si and the conductive network and solves the poor conductivity problem of Si, which is known as a semiconductor material. This unique configuration design of CuNW@Si@C-400 °C leads to stable long cycle performance of 1109 mAh·g^{-1} after 1000 cycles and excellent rate performance of 500 mAh·g^{-1} at a current density of 10 A·g^{-1}. Furthermore, the CuNW@Si@C-400 °C||$LiFePO_4$ (LFP) full battery demonstrates excellent flexibility, with a capacity retention of more than 96% after 100 bends. This study provides a promising strategy for the development of flexible lithium-ion batteries.

KEYWORDS

flexible lithium-ion battery, silicon anode, magnetron sputtering, core–shell electrode, Cu nanowire array

1 Introduction

With the significant increase in the application of portable electronic devices and smart wearable electronic devices, the demand for high power-density flexible lithium-ion batteries (LIBs) is growing rapidly [1–3]. However, there are many challenges in developing flexible lithium-ion batteries. On the one hand, during the bending processes, the stress can lead to the structural collapse of electrodes, breakage of the conductive network, and material peeling off the collector [4]. On the other hand, a thinner battery is needed for better bendability [5–7], implying that active materials with high specific or volume capacity are the best choice [8–10]. Silicon is an abundantly available anode material that has a theoretical gravimetric capacity of 3579 mAh·g^{-1}, a theoretical volumetric capacity of 8322 mAh·L^{-1}, and a low operating potential of 0–0.4 V vs. Li/Li$^+$ [11, 12]. Therefore, silicon is considered as the most promising candidate for the next generation of flexible LIBs anodes [13–17]. However, during the lithiation and delithiation processes, silicon suffers from large volume variation (≈ 300%) that leads to pulverization, causing delamination from the conductive network [18–22]. Continuous generation of fracture surfaces will continuously consume lithium-ions to generate solid electrolyte interphase (SEI), resulting in the specific capacity decay [23–25]. Moreover, silicon is a semiconductor material, and its electrical conductivity is far from traditional graphite material. Some particles lose contact with the conductive network and cannot provide capacity [26]. How to achieve both electrochemical and mechanical stability in the dynamic and bending state of the flexible battery is a great challenge.

So far, there have been a lot of research results on flexible silicon anode electrodes such as Si/carbon nanotube (CNT) film [12, 27–30], Si/graphene paper [31–33], Si/MXene [34–40], or developed flexible binders [41–45]. The design and application of carbon nanomaterials and functional bonding agents can effectively improve the mechanical properties of Si anodes. However, currently prepared carbon materials often contain a high number of defects, which make them impossible to provide satisfactory electron conduction in Li-ion battery applications as well as more irreversible lithium losses in the first cycle. Meanwhile some recent works prepared ionic conductive binders based on PAA or other carboxylate type polymers by Li-ion

Address correspondence to Xiang Han, hanxiang@njfu.edu.cn; Wei Huang, weihuang@xmu.edu.cn; Songyan Chen, sychen@xmu.edu.cn

exchange [46–48], but strong Lewis acid–based interaction between carboxylate groups and lithium ions limited their conduction capability. Therefore, although the various strategies mentioned above have improved the electrochemical properties of silicon and the mechanical properties of electrodes to some extent, there are still embarrassing situations such as high costs, complicated processes, and less than ideal electrode performance. From this point of view, designing a structure that can tolerate the stress of electrode bending without breaking, and at the same time building a continuous, stable, and high-speed network of electron channels is the key to developing flexible lithium-ion batteries.

Herein, we propose a nanowire (NW) array structure with an alloy transition layer at the Cu/Si interface. The preparation of this electrode structure is carried out by simple and proven means. The anodic oxidation, annealing, and magnetron sputtering used in the process can be carried out in uniform batches. We also propose the idea of annealing and alloying the Cu/Si interface to form a unique conductive and adhesive agent to give the electrode excellent cycling stability and rate performance. Meanwhile, the nanowire array structure can greatly alleviate the stress accumulation phenomenon during the bending process and release the stress through the bending and twisting of nanowires themselves, which is conducive to the development of flexible and bendable electrodes. This concept is further confirmed in the finite element analysis.

2 Experimental

2.1 Synthesis

2.1.1 *Preparation of CuNWs on Cu foil*

Copper hydroxide nanowire arrays were fabricated on copper foil by electrochemical anodizing. To remove the oxide layer and stains on the surface, the copper foil was ultrasonically washed in 5% hydrochloric acid (HCl) solution for 10 min, followed by rinsed with deionized water. Next, the copper foil was immersed in 1 M potassium hydroxide (KOH) solution, and a constant voltage source was set to 1.2 V. The anode was connected to the copper foil and the cathode was connected to a platinum electrode for 10 min. Afterward, the copper foil was washed with deionized water and transferred to a tube furnace for annealing and reduction. Using an argon–hydrogen mixture (5% H_2) at a flow rate of 20 sccm, the temperature was set to 400 °C and the samples were annealed for 30 min with a ramping rate of 5 °C·min^{-1}.

2.1.2 *Synthesis of CuNW@Si@C-400 °C on Cu foil*

The CuNWs obtained from the previous step were used for further processing. The CuNWs were placed in a magnetron sputtering machine, and the air pressure was set to 1.0 Pa, while the argon flow rate was set to 15 sccm. The polysilicon target was sputtered with a radio frequency (RF) power supply set at 100 W for 60 min, then the graphite target was sputtered with a direct current (DC) power supply set at 50 W for 30 min. The vacuum was maintained in the magnetron sputtering machine, and the obtained CuNW@Si@C sample was gradually increased to 400 °C at a rate of 5 °C·min^{-1}.

2.2 Characterization

The samples were characterized using scanning electron microscopy (SEM, Zeiss Sigma, 10 kV), transmission electron microscopy (TEM, Philips Tecnai F30), X-ray photoelectron spectroscopy (XPS, PHI 5000 Versaprobe III), and X-ray diffraction (XRD, Rigaku Ultima IV with Cu Kα radiation). The active mass was weighed using a microbalance (METTLER TOLEDO XS3DU), and the IV characteristics were measured using a digital source-meter (Keithley, 2611B).

2.3 Electrochemical test

To assess the electrochemical performance of CuNW@Si@C, a CR2025 coin cell was assembled in a glovebox (Mbraun, LABmaster 100, Germany, H_2O, O_2 < 0.1 ppm) with a lithium foil serving as the counter electrode. The electrolyte solution comprised 1 M $LiPF_6$ in ethylene carbonate (EC), dimethyl carbonate (DMC), and diethyl carbonate (DEC) (1:1:1 in volume) with 10% fluorinated ethylene carbonate (FEC) additive. The half-cells were tested over a voltage range of 0.005–1.5 V vs. Li/Li$^+$ at room temperature using a Land CT2001A system (Wuhan, China). The electrochemical impedance spectroscopy (EIS) was performed from 1 MHz to 0.01 Hz with 5 mV of amplitude on an electrochemical workstation (Shanghai Chenhua, CHI 604E). To fabricate the electrode for the flexible battery, CuNW@Si@C-400 °C was cut into long strips (1.5 cm × 3 cm), and cathode electrodes consisting of $LiFePO_4$ (LFP), super P, and polyvinylidene fluoride (PVDF) were prepared (80:10:10 by weight). The full cells were designed with an N/P ratio of 1.1 and laminated in aluminum plastic film. The CuNW@Si@C-400 °C anodes were first prelithiated using half-cells at 0.2 A·g^{-1} for two cycles to form a stable SEI, and then the full-cell tests were carried out in the voltage window between 2.0 and 4.2 V. The calculation of the masses of the active substances is mentioned in Figs. S3 and S4 and Tables S1–S4 in the Electronic Supplementary Material (ESM).

2.4 Simulation

The bending deformation of the integrated CuNW@Si@C-400 °C electrode structure was simulated using the finite element method implemented in ABAQUS software. The material was modeled as isotropic with an elastic modulus and Poisson's ratio. The Cu foil@Si@C-400 °C electrode interface was assumed to be in "hard contact" in the normal direction and "rough" in the tangential direction. The simulation applied a completely fixed boundary at one end of the electrode and a fixed pressure at the other end. The meshing was performed using freely divided tetrahedra with standard properties, and the improved formula calculation was used. The analysis step was set as "static, general, and geometric nonlinearity".

3 Results and discussion

Figure 1 illustrates the synthetic route for CuNW@Si@C-400 °C. First, the copper foil was anodized with a KOH solution (Fig. 1(a)). The oxidized copper foil was then annealed and reduced to obtain copper nanowires (Fig. 1(b)). Subsequently, the surface of the copper nanowires was coated with Si and C by magnetron sputtering and annealed *in situ* according to the appropriate parameters (Fig. 1(c)). The sample has a large number of nanowires that are grown vertically on top of the copper foil. This structure offers several advantages, including shorter lithium-ion diffusion paths and increased silicon loading per unit area due to the silicon coating on the vertical copper nanowire surface. In addition, the nanowire array structure has the important property of eliminating stress accumulation. During cycling, silicon undergoes a dramatic volume expansion (~ 300%), which can be accommodated by the space between the discrete nanowires. Individual nanowires are free to release stresses by bending and twisting, thus maintaining the stability of the electrode structure. Figure 1(d) shows a schematic diagram of a single nanowire profile, which depicts the ability of the electrode to keep the microscopic nanowire array stable during macroscopic bending

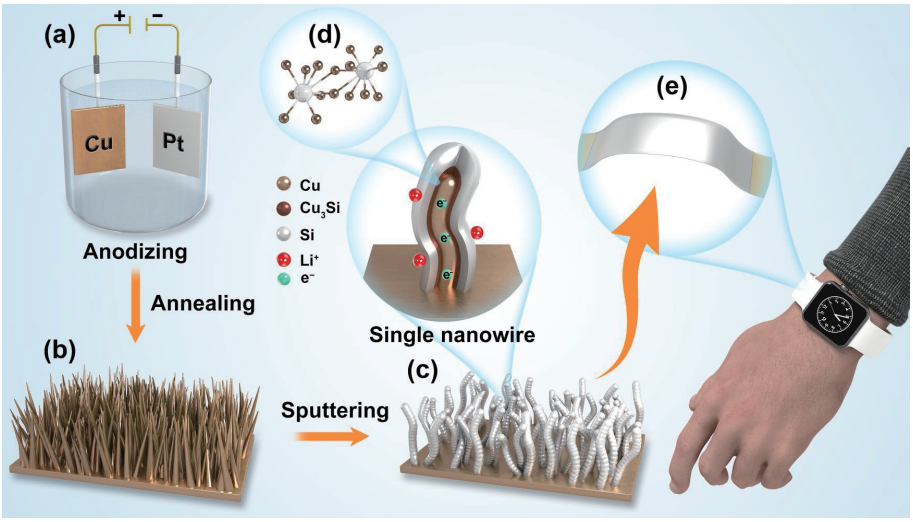

Figure 1 Schematic diagrams of the process of preparing CuNW@Si@C-400 °C. (a) Preparation of $Cu(OH)_2$ nanowire arrays by anodic oxidation. (b) Cu nanowire arrays were obtained by annealing reduction. (c) Magnetron sputtering covers the active material and anneals it *in situ* to produce a Cu_3Si alloy. (d) Schematic diagram of the nanowire profile. The intermediate Cu and the outer Si layer are anchored by a Cu_3Si alloy interfacial layer. (e) Nanowire array electrodes can be used to build flexible energy storage devices.

and deformation. Using this feature, a bendable lithium-ion battery can be developed (Fig. 1(e)). At the same time, the schematic diagram illustrates the design idea behind this structure: The internal Cu acts as an excellent electron channel for fast electron transfer, which is essential for improving the electrochemical properties of Si. The external sputtered Si and C act as the active material and the protective layer, respectively. Heating at the Si/Cu interface leads to the formation of a small amount of Cu_3Si alloy. The Cu_3Si alloy transition layer enhances the electron transfer properties from Cu to Si and holds the Si firmly on the Cu surface, preventing it from dislodging easily.

To confirm the successful fabrication of CuNW@Si@C-400 °C mentioned above, a range of material characterizations were conducted. Figure 2(a) displays the anodized copper foil treated with potassium hydroxide, revealing a dense growth of "spines" on its surface. Subsequent XRD analysis identified these spine-like structures as $Cu(OH)_2$, which acted as the precursor for the electrode microstructure and influenced the final size of the single nanowires. A cross-sectional view in Fig. 2(b) shows the dimensions of the $Cu(OH)_2$ nanowires to be around 50 nm in diameter and 8 μm in length, with a straight overall morphology that is slightly thicker at the bottom. In Fig. 2(c), the nanowire array structure is shown to remain intact after the annealing reduction process, with the single nanowires slightly bent due to stress. Importantly, the array structure has enough space to accommodate the bending of the nanowires, effectively releasing stresses and ensuring mechanical stability, which is vital during the cell cycling process. Figure 2(d) depicts the final electrode morphology after magnetron sputtering and annealing, where each copper nanowire is uniformly coated with Si and C layers at its periphery. The sample was also observed morphologically by TEM (Fig. S1 in the ESM). The nanowire was wrapped with a uniform thickness shell from top to bottom. To verify and analyze the Cu/Si interface composition, selected area electron diffraction (SAED) test was performed. The presence of Cu_3Si (030) and Cu (220) components can be obtained from the brightness integral spectrum of diffraction. Meanwhile, Raman spectroscopy tests were used to verify the outermost C coating (Fig. S2 in the ESM). The characteristic peak of amorphous silicon can be clearly seen at 500 cm^{-1}, and the D and G peaks representing C appear at 1300 and 1600 cm^{-1}. The single nanowire measures approximately 400 nm in diameter and 8 μm in length, and the sputtered layer only adheres to the surface of the nanowire, leaving sufficient space to accommodate the expansion and bending of Si. Additionally, energy dispersive spectroscopy (EDS) mapping images of the electrodes in Figs. 2(e)–2(h) confirm the uniformity of the coating achieved by magnetron sputtering, with each nanowire region exhibiting a strong Si and C signal while the Cu signal decreasing significantly. This suggests that the Si and C particles are preferentially deposited on the surface of the Cu nanowires, rather than directly on the root to form a plane. With its conformal coating property, magnetron sputtering shows significant promise for coating processing in the micro and nano materials field.

The lack of interaction between magnetron-sputtered Si and CuNW increases the likelihood of losing connection to the conductive network due to Si exfoliation, compared with conventional adhesive formulations. To address this issue, the Si and Cu were heated to form a compound that would bond to each other, thus increasing contact strength. XRD and XPS tests were conducted to verify whether the annealing process produced a trace Cu_3Si alloy. Figure 2(i) shows the red, gray, and blue curves representing copper hydroxide nanowire samples after anodic oxidation, copper nanowire samples after annealing reduction, and electrode samples after magnetron sputtering and annealing, respectively. Since all samples were placed on copper foils, the three strongest peaks observed were all diffraction peaks of Cu, namely (111), (200), and (220) peaks. However, the $Cu(OH)_2$ (020) and (021) peaks at 16.7° and 23.8° respectively, appeared only in the sample after anodic oxidation (red curve), indicating that Cu loses electrons to Cu^{2+} under the anodic action of a constant voltage source and immediately binds with OH^- in solution to form nanowire-like deposits.

Subsequently, the copper hydroxide nanowires were annealed in a tube furnace by passing a mixture of argon–hydrogen gas. They were first thermally decomposed into CuO nanowires and then reduced to Cu nanowires. At this point, the XRD peaks of the Cu nanowire sample (gray curve) retained only the three peaks belonging to Cu, while the two peaks previously belonging to $Cu(OH)_2$ disappeared. The Cu nanowires were then coated with Si and C by magnetron sputtering and vacuum annealed directly in the cavity. The diffraction pattern of the sample (blue curve) still mainly showed the three diffraction peaks of Cu, with a weak diffraction peak at 36.6° (shown in the inset) corresponding to Cu_3Si (201). This weak diffraction peak was intentionally generated by controlling the annealing temperature and time to

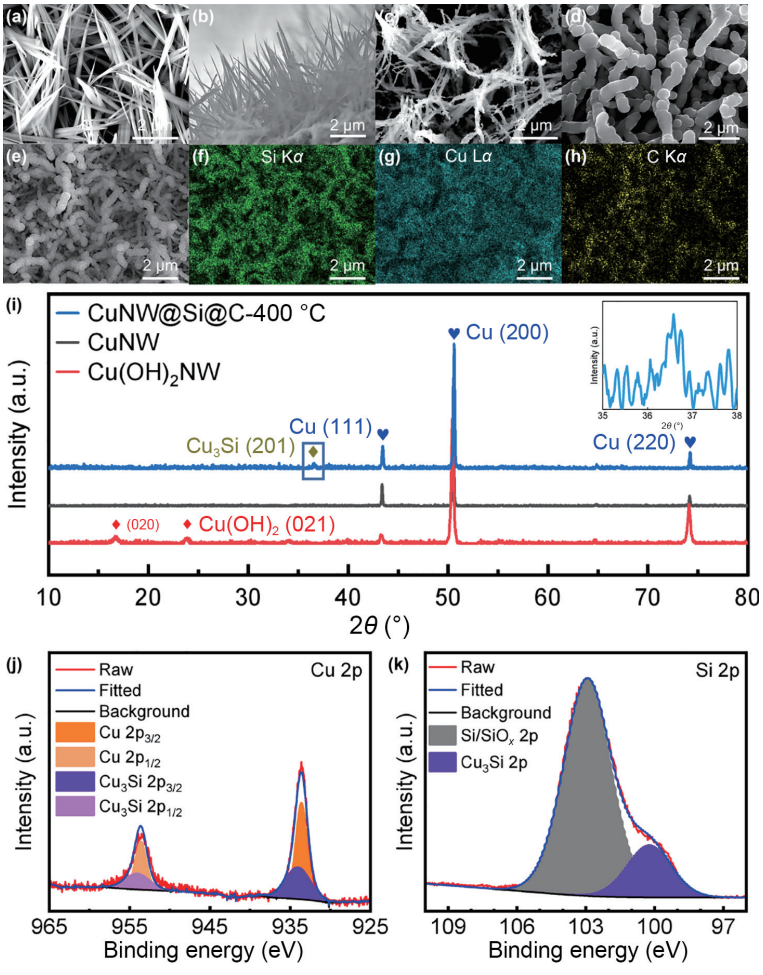

Figure 2 Physical characterization of CuNW@Si@C-400 °C electrode. (a) SEM image of $Cu(OH)_2$. (b) Cross-sectional SEM image of $Cu(OH)_2$. (c) SEM image of CuNW. (d) SEM image of CuNW@Si@C-400 °C electrode. (e)–(h) EDS mapping images of Si, Cu, and C elements in CuNW@Si@C-400 °C electrode. (i) XRD patterns of $Cu(OH)_2$, CuNW, and CuNW@Si@C-400 °C. (j) XPS spectra of Cu 2p orbitals of CuNW@Si@C-400 °C. (k) Si 2p orbital XPS spectra of CuNW@Si@C-400 °C.

avoid excessive Si alloying that would consume the active material. It's important to note that the diffraction peak of Cu is too strong when measured on a copper foil substrate.

To further confirm the generation of the Cu_3Si alloy, XPS tests were performed on the samples. Both the $2p_{3/2}$ and $2p_{1/2}$ orbitals of Cu showed a small shift toward higher binding energy, and after split-peak fitting, it was found that the Cu $2p_{3/2}$ orbital had a peak corresponding to 933.7 eV of Cu and a peak corresponding to 934.1 eV of Cu_3Si. The Cu $2p_{1/2}$ orbital auto-fit curve also showed a good match. The same split-peak fits were done for the 2p orbitals of Si. The binding peaks of Si/SiO_x and Cu_3Si at 102.8 and 99.1 eV, respectively, were exhibited and fitted well.

To assess the impact of Cu_3Si alloying on the electrochemical performance of Si anodes, two control electrodes were prepared: CuNW@Si@C with only a nanowire array and Cu foil@Si@C-400 °C with only Cu_3Si alloy. These electrodes were assembled in a coin cell and subjected to two cycles of activation at 0.2 $A{\cdot}g^{-1}$ before being cycled at 2 $A{\cdot}g^{-1}$ current density. The reported specific capacities are based on the total mass of the composite electrode material. The CuNW@Si@C electrode, lacking the anchoring effect of Cu_3Si, showed poor cycling performance due to the active materials peeling off from the CuNW surface. The large surface area of nanowire arrays leads to continuous side reactions during repeated lithiation/delithiation processes. The initial specific capacity was 2470 $mAh{\cdot}g^{-1}$, but it rapidly decreased to 750 $mAh{\cdot}g^{-1}$ at the 100th cycle and to 296 $mAh{\cdot}g^{-1}$ at the 500th cycle, with a capacity retention rate of only 12%. In contrast, the Cu foil@Si@C-400 °C electrode showed a more stable cycle than SiNW, with an initial specific capacity of 2130 $mAh{\cdot}g^{-1}$ and a capacity retention rate of 23% after 600 cycles of 504 $mAh{\cdot}g^{-1}$. This improved cycling performance is attributed to the anchoring effect of Cu_3Si and the smaller surface area, which lead to weaker side reactions. However, the planar structure of the electrode accumulates stress as the volume expands, eventually resulting in electrode structure collapse and powder, which further deteriorates cycling performance. The presence of Cu_3Si alloy enhances the electrical conductivity of the nanowires, and the chemically inert Cu_3Si alloy serves as a contact point, making it difficult to separate the outer Si from CuNW during the lithiation/delithiation processes, which improves structural stability.

In the CuNW@Si@C-400 °C electrode, a high-speed conductive frame and strong contact structure were established using Cu_3Si as a conductive agent and adhesive. This electrode had an initial specific capacity of 1908 $mAh{\cdot}g^{-1}$, and after 1000 cycles, it retained a capacity of 1109 $mAh{\cdot}g^{-1}$, with a capacity retention rate of 58%.

Figure 3(b) illustrates the galvanostatic discharge–charge curves of the CuNW@Si@C-400 °C electrode. The initial discharge specific capacity and charge specific capacity are 1905 and 1462 $mAh{\cdot}g^{-1}$, respectively, resulting in an initial Coulombic efficiency of 76%. The reduction in charge capacity can be mainly attributed to the side reactions between the Si negative electrode and Li ions, as well as the formation of SEI on the electrode surface. The discharge voltage plateau ranges from 0.3–0 V, while the charging voltage plateau ranges from 0.2–0.5 V, corresponding to the characteristic charge/discharge plateau of Si. After a few initial cycles, the curve shape and charge/discharge plateau remain

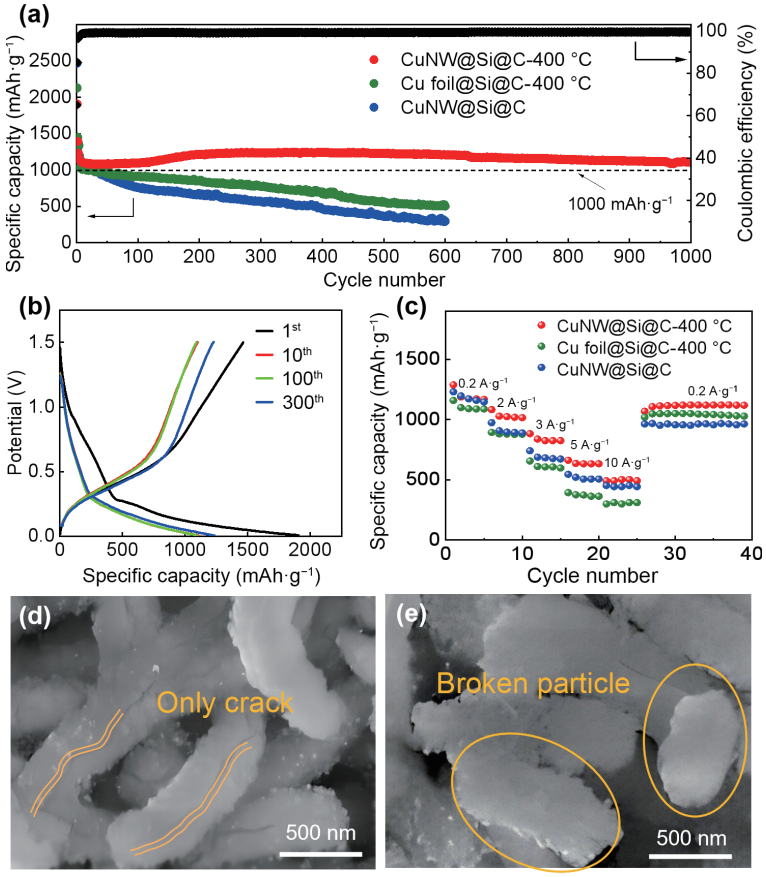

Figure 3 Half-cell electrochemical performance tests. (a) Cycle performance of three different electrodes. (b) Specific capacity–potential curves of CuNW@Si@C-400 °C. (c) Rate performance of three different electrodes. (d) SEM image of CuNW@Si@C-400 °C electrode after 500 cycles. (e) SEM image of CuNW@Si@C electrode after 500 cycles.

relatively stable at the 10th and the 100th cycles, indicating the excellent electrochemical stability of the CuNW@Si@C-400 °C electrodes. By the 300th cycle, the charge/discharge plateau remained unchanged, but the specific capacity increased slightly, indicating the full activation of the nanowire structure and excellent electrode stability.

Figure 3(b) illustrates voltage versus specific capacity profiles of CuNW@Si@C-400 °C electrodes. During discharge, a voltage plateau appears at 0.3–0 V, which then transforms into a sloping line with a fixed slope. Similarly, during charging, a voltage plateau appears at 0.2–0.5 V, also forming a diagonal line. These voltage ranges are consistent with the charging and discharging characteristics of silicon, and are also in line with the cyclic voltammetry (CV) results. Notably, due to silicon becoming amorphous during the magnetron sputtering process, there is no horizontal voltage platform. In the 10th and the 100th cycles, the curves show good agreement, indicating good electrochemical stability of the electrode. Between the 100th and the 300th cycles, a slight increase in capacity is observed due to the nanostructure undergoing an electrode activation process along with the cycle. When the capacity increase of the activation process exceeds the circulation capacity decline, there is a capacity increase phenomenon.

The three electrodes were tested for their rate performance, as shown in Fig. 3(c). The CuNW@Si@C-400 °C electrode maintains the highest performance across the current densities ranging from 0.2 to 10 $A·g^{-1}$. At 0.2 $A·g^{-1}$, the specific capacity of CuNW@Si@C-400 °C electrode is 1186 $mAh·g^{-1}$, and even at a higher current density of 10 $A·g^{-1}$, the specific capacity remains as high as 491 $mAh·g^{-1}$. Moreover, when the current density decreases to 0.2 $A·g^{-1}$, the electrode immediately recovers to a specific capacity of 1120 $mAh·g^{-1}$. In contrast, the Cu foil@Si@C-400 °C electrode exhibits a larger capacity decay at higher current densities, possibly due to its planar structure with a smaller specific surface area and fewer Li ion insertion/extraction pathways. The CuNW@Si@C electrode, with its nanowire array structure and more Li ion channels, performs better at high current density conditions. However, it does not recover the specific capacity as well as the Cu foil@Si@C-400 °C electrode after returning to the current density of 0.2 $A·g^{-1}$. This might be due to the insufficient interaction between Si and Cu, resulting in some active material detachment from the conducting network during cycling and forming isolated islands. These results indicate that the nanowire array structure can increase Li transit channels and shorten the electron transport path in Si, and the presence of Cu_3Si alloy provides an additional safeguard to the structural stability. The CuNW@Si@C-400 °C and Cu foil@Si@C-400 °C electrodes were opened after 500 cycles and observed under a scanning electron microscope. It can be seen that the structure of the CuNW@Si@C-400 °C electrode is very robust, with no active material or copper nanowires falling off except for some cracks caused by volume expansion/contraction on the surface (Fig. 3(d)). However, a large number of particles were observed to fracture and detach from the nanowire structure in the Cu foil@Si@C image (Fig. 3(e)). These phenomena are easily understood in our electrode model. A small amount of alloying substance is produced between Si and Cu through annealing at a certain temperature and time, which greatly increases the interaction between Si and Cu. Moreover, Cu_3Si does not have lithium storage activity and remains inert during cycling, firmly holding onto Si. Electrodes without Cu_3Si will continue to fracture, and these new fracture surfaces will produce more SEI films and easily lose electrical contact, which is the main reason for performance degradation.

To further investigate the performance differences among the

three electrodes and to confirm the superiority of the CuNW@Si@C-400 °C electrode, we conducted CV and EIS tests. During the CV test, we widened the electrochemical cycling voltage range to 0–3 V to fully and clearly display all the characteristic peaks of the CuNW@Si@C-400 °C electrode, as shown in Fig. 4(a). During the reduction process of the first lap (red curve), a faint characteristic peak appears at 1.2 V, which does not have a corresponding oxidation peak. Based on several Si anode papers, we conclude that this peak is caused by the SEI during the first cycle, indicating the good stability of electrodes and reduced likelihood of new Si exposure during cycling due to structural rupture and subsequent repeated SEI formation. However, the nanowire array structure has a large specific surface area and has a low Coulombic efficiency during the first cycle. Therefore, it can be seen that there are strong characteristic peaks around 0 V during the reduction process, but not strong enough to appear during the oxidation process. In the later CV curves, the potential of the redox peak in the CV curves does not change. The reduction peaks always remain at around 0 and 0.2 V. The oxidation peaks always remain at around 0.3 and 0.5 V. Moreover, the characteristic peaks increase with the number of cycles. This is because the electrode material is gradually activated during the cycling process and more active substances are involved in the reaction. After 500 cycles, we performed the cyclic voltammetry test again, as shown in Fig. 4(b). The cell exhibits a very standard characteristic peak and is more pronounced than the characteristic peak of the second cycle. There are two reduction peaks at 0–0.2 V and two oxidation peaks at 0.4–0.6 V, corresponding to the two-phase process of Si lithiation/delithiation. After 500 cycles, we performed cyclic voltammetry tests again, as shown in Fig. 4(b). The cell exhibits a very standard characteristic peak, with two reduction peaks at 0–0.2 V and two oxidation peaks at 0.4–0.6 V, corresponding to the two-phase process of Si lithiation/delithiation. Interestingly, the curves obtained from the two scans before and after overlap very well, indicating that the electrochemical behavior of the CuNW@Si@C-400 °C electrode is highly stable.

We also conducted EIS tests on the three electrodes, and the results are shown in Fig. 4(c). After 100 cycles, significant differences in the EIS of the three electrodes were observed, with the CuNW@Si@C-400 °C electrode exhibiting the smallest charge transfer impedance (R_{ct} = 27 Ω) due to the excellent conductive network of the Cu-Si alloy and higher surface area of the nanowire structure. In contrast, the CuNW@Si@C electrode lacks a Cu_3Si transition layer, resulting in a disadvantage in electron transport, with a charge transfer impedance of approximately 82 Ω. The Cu foil@Si@C-400 °C electrode, a planar structure with a much smaller surface area than the nanowire array structure, exhibits the largest charge transfer impedance (approximately 142 Ω). In conclusion, the nanowire array structure and Cu_3Si alloy can improve the lithium-ion transfer impedance of the electrode.

We also conducted EIS tests on the CuNW@Si@C-400 °C electrode after different cycles, as shown in Fig. 4(d). The charge transfer impedance of the electrode after the 10th cycle is approximately 50 Ω, which decreases to 27 Ω after an electrode activation process following the hundredth cycle. After the third hundredth cycle, the charge transfer impedance slightly increases to 40 Ω. These results demonstrate the excellent stability of the CuNW@Si@C-400 °C electrode structure, which is consistent with the high anastomosis observed in Fig. 3(a).

To evaluate the performance of CuNW@Si@C-400 °C electrodes in full batteries, we assembled full batteries with $LiFePO_4$ cathodes. Figure 5(a) shows the constant current charge–discharge curves in the potential range of 2.0–4.2 V vs. Li/Li^+ at a current density of 2 $A{\cdot}g^{-1}$. After 100 cycles, the discharge capacity remained at 56%. Figure 5(b) shows that the capacity loss was less than 4% after bending the electrode 100 times, and the charge–discharge voltage levels were consistent before and after bending. This indicates that the CuNW@Si@C-400 °C electrode has good mechanical stability and can be applied in wearable smart devices. As shown in Fig. 5(c), a flexible pouch cell was fabricated that can withstand bending and continuously light up a set of light-emitting diode (LED) bulbs.

To demonstrate the applicability of the CuNW@Si@C-400 °C electrode structure in the development of flexible cells, we developed a finite element analysis model and conducted mechanical simulations. As depicted in Fig. 6(a), the control group consists of an upper planar layer coated with conventional

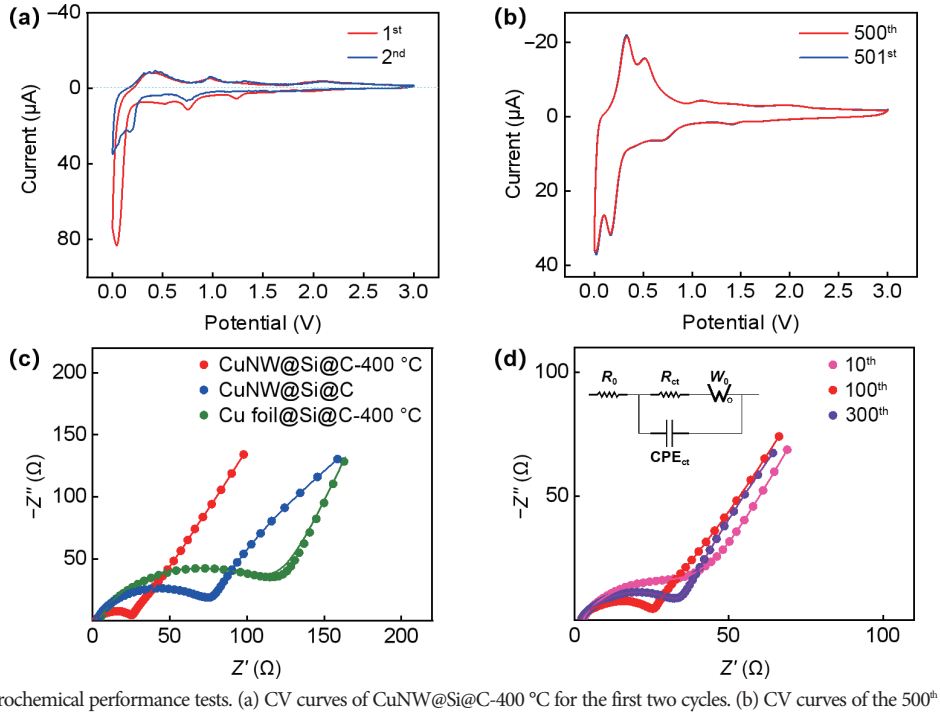

Figure 4 Half-cell electrochemical performance tests. (a) CV curves of CuNW@Si@C-400 °C for the first two cycles. (b) CV curves of the 500th and the 501st cycles. (c) EIS spectra of three different electrodes after 100 cycles. (d) EIS spectra of CuNW@Si@C-400 °C electrodes at the 10th, 100th, and 300th cycles.

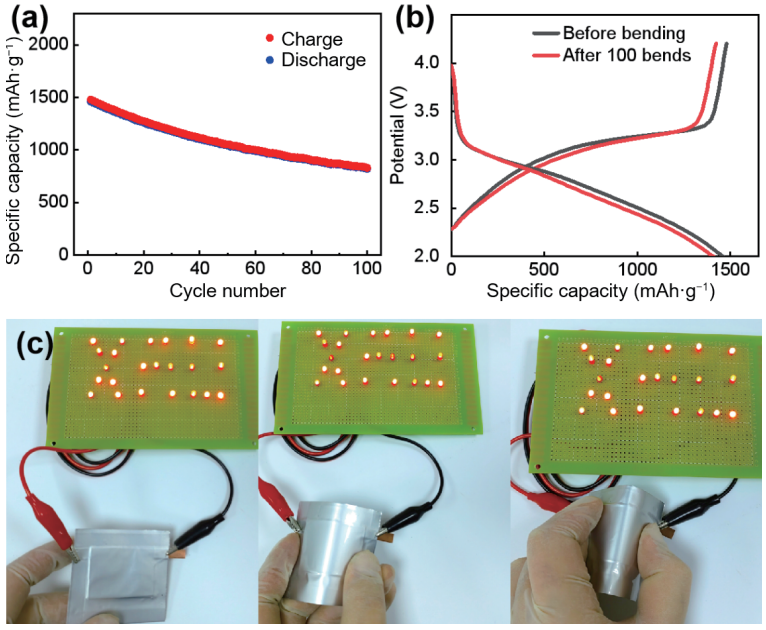

Figure 5 (a) Cyclic specific capacity performance of the CuNW@Si@C-400 °C||$LiFePO_4$ battery. (b) Charge/discharge plateau diagrams of the CuNW@Si@C-400 °C||$LiFePO_4$ cell. (c) Flexible pack battery drives the LED bulb group to work.

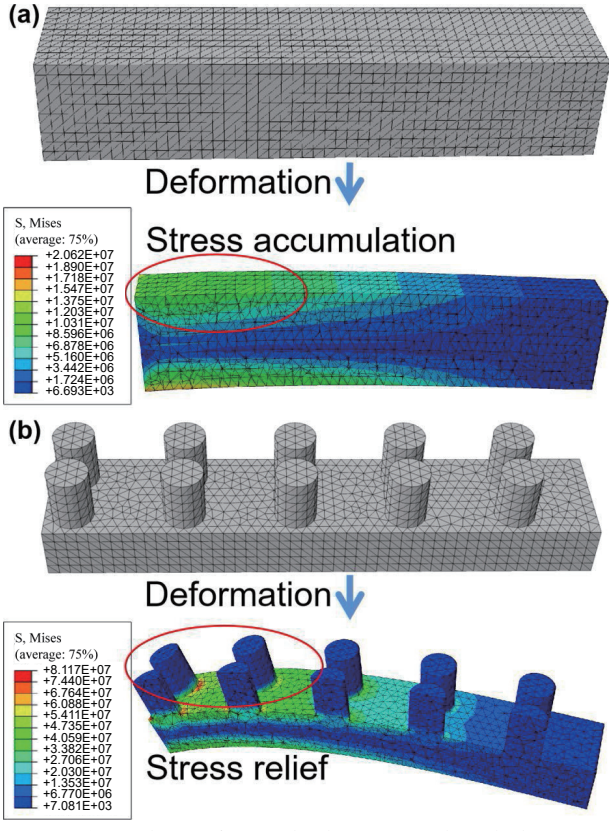

Figure 6 (a) Simulation of stress distribution in traditional plane coating process. (b) Simulation of stress distribution in nanowire array structures.

adhesive on the collector. In contrast, the CuNW@Si@C-400 °C electrode structure in Fig. 6(b) has nanowires grown *in situ* on the Cu collector at the same height. During the bending process, stress concentration occurs in some regions of the conventional electrode, making it highly susceptible to structural fracture. The active material in the fractured region loses contact with the collector and the conducting network, leading to a deterioration in performance. In more severe cases, the fractured material can pierce the diaphragm, eventually causing a short circuit in the battery and potentially resulting in accidents such as fire. In contrast, the nanowire structure on the right side of Fig. 6(b) prevents stress accumulation in the active material region, thereby reducing stress levels by three orders of magnitude compared with the control group. This stress reduction is crucial for the development of flexible electrodes, especially for silicon-based anodes, which experience internal stresses due to drastic volume changes during cycling. The nanowire structures separation property effectively mitigates these stresses, ensuring the stability and reliability of the electrode during operation.

4 Conclusions

In summary, we have fabricated a CuNW@Si@C-400 °C nanowire array anode structure for flexible lithium-ion batteries. The electrodes were prepared by anodic oxidation and magnetron sputtering methods, and were easy to prepare in large-area batches. After cutting into the desired shape, it could be used for lithium-ion battery anodes. Thanks to the high electron conductivity of the Cu core in the nanowire structure and the solid contact of Cu_3Si, the semiconductor material properties of Si are greatly improved, effectively enhancing cycle life and rate performance. The initial cycle capacity is 2856 mAh·g^{-1}, and the capacity after 1000 cycles is 1602 mAh·g^{-1} (i.e., 60% retention). The specific capacity is maintained at 491 mAh·g^{-1} at a current density of 10 A·g^{-1}. The nanowire structure reserves buffer space for volume changes during Si cycling and releases stress in the active material region during deformation of the electrode. This allows the electrode structure to have a long-term stable cycle and withstand hundreds of times of bending deformation while still maintaining its capacity. The good electrochemical performance of CuNW@Si@C-400 °C shows that the core–shell nanowire arrays coupled with "inert" metal silicides as conductive and binder electrode material design can help drive the next generation of high-performance flexible lithium-ion batteries.

Acknowledgements

Financial supports from the National Natural Science Foundation of China (No. 22209075), the Natural Science Foundation of Chongqing (No. 2022NSCQ-MSX4268), the Postdoctoral Innovation Talents Support Plan of Chongqing (No. CQBX2021012), and the Scientific Research Project of Fujian Provincial Department of Education (No. JAT220530) are acknowledged.

Electronic Supplementary Material: Supplementary material (TEM images, SAED pattern, Raman spectrum, and means of measuring active materials) is available in the online version of this article at https://doi.org/10.1007/s12274-023-5982-6.

References

[1] Zuo, X. X.; Zhu, J.; Müller-Buschbaum, P.; Cheng, Y. J. Silicon based lithium-ion battery anodes: A chronicle perspective review. *Nano Energy* **2017**, *31*, 113–143.

[2] Liu, J.; Bao, Z. N.; Cui, Y.; Dufek, E. J.; Goodenough, J. B.; Khalifah, P.; Li, Q. Y.; Liaw, B. Y.; Liu, P.; Manthiram, A. et al. Pathways for practical high-energy long-cycling lithium metal batteries. *Nat. Energy* **2019**, *4*, 180–186.

[3] Liu, Q.; Hu, Y. H.; Yu, X. R.; Qin, Y. F.; Meng, T.; Hu, X. L. The pursuit of commercial silicon-based microparticle anodes for advanced lithium-ion batteries: A review. *Nano Res. Energy* **2022**, *1*, e9120037.

[4] Choi, S.; Kwon, T. W.; Coskun, A.; Choi, J. W. Highly elastic binders integrating polyrotaxanes for silicon microparticle anodes in lithium ion batteries. *Science* **2017**, *357*, 279–283.

[5] Chang, J.; Huang, Q. Y.; Gao, Y.; Zheng, Z. J. Pathways of developing high-energy-density flexible lithium batteries. *Adv. Mater.* **2021**, *33*, e2004419.

[6] Xiang, F. W.; Cheng, F.; Sun, Y. J.; Yang, X. P.; Lu, W.; Amal, R.; Dai, L. M. Recent advances in flexible batteries: From materials to applications. *Nano Res.* **2023**, *16*, 4821–4854.

[7] Xu, T.; Du, H. S.; Liu, H. Y.; Liu, W.; Zhang, X. Y.; Si, C. L.; Liu, P. W.; Zhang, K. Advanced nanocellulose-based composites for flexible functional energy storage devices. *Adv. Mater.* **2021**, *33*, e2101368.

[8] Sun, L.; Liu, Y. X.; Shao, R.; Wu, J.; Jiang, R. Y.; Jin, Z. Recent progress and future perspective on practical silicon anode-based lithium ion batteries. *Energy Storage Mater.* **2022**, *46*, 482–502.

[9] Sun, L.; Xie, J.; Huang, S. C.; Liu, Y. X.; Zhang, L.; Wu, J.; Jin, Z. Rapid CO_2 exfoliation of Zintl phase $CaSi_2$-derived ultrathin free-standing Si/SiO_x/C nanosheets for high-performance lithium storage. *Sci. China Mater.* **2022**, *65*, 51–58.

[10] Xie, J.; Sun, L.; Liu, Y. X.; Xi, X. G.; Chen, R. Y.; Jin, Z. SiO_x/C-Ag nanosheets derived from zintl phase $CaSi_2$ via a facile redox reaction for high performance lithium storage. *Nano Res.* **2022**, *15*, 395–400.

[11] Chen, M.; Zhou, Q. N.; Zai, J. T.; Iqbal, A.; Tsega, T.; Dong, B. X.; Liu, X. J.; Zhang, Y. C.; Yan, C. Y.; Zhao, L. et al. High power and stable P-doped yolk–shell structured Si@C anode simultaneously enhancing conductivity and Li^+ diffusion kinetics. *Nano Res.* **2021**, *14*, 1004–1011.

[12] Zhang, Q. L.; Xi, B. J.; Chen, W. H.; Feng, J. K.; Qian, Y. T.; Xiong, S. L. Synthesis of carbon nanotubes-supported porous silicon microparticles in low-temperature molten salt for high-performance Li-ion battery anodes. *Nano Res.* **2022**, *15*, 6184–6191.

[13] Ge, M. Z.; Cao, C. Y.; Biesold, G. M.; Sewell, C. D.; Hao, S. M.; Huang, J. Y.; Zhang, W.; Lai, Y. K.; Lin, Z. Q. Recent advances in silicon-based electrodes: From fundamental research toward practical applications. *Adv. Mater.* **2021**, *33*, e2004577.

[14] Li, P.; Kim, H.; Myung, S. T.; Sun, Y. K. Diverting exploration of silicon anode into practical way: A review focused on silicon-graphite composite for lithium ion batteries. *Energy Storage Mater.* **2021**, *35*, 550–576.

[15] Vijayakumar, V.; Anothumakkool, B.; Kurungot, S.; Winter, M.; Nair, J. R. *In situ* polymerization process: An essential design tool for lithium polymer batteries. *Energy Environ. Sci.* **2021**, *14*, 2708–2788.

[16] Wang, F.; Wang, B.; Li, J. X.; Wang, B.; Zhou, Y.; Wang, D. L.; Liu, H. K.; Dou, S. X. Prelithiation: A crucial strategy for boosting the practical application of next-generation lithium ion battery. *ACS Nano* **2021**, *15*, 2197–2218.

[17] Zhao, X. Y.; Lehto, V. P. Challenges and prospects of nanosized silicon anodes in lithium-ion batteries. *Nanotechnology* **2021**, *32*, 042002.

[18] Liu, Z. H.; Yu, Q.; Zhao, Y. L.; He, R. H.; Xu, M.; Feng, S. H.; Li, S. D.; Zhou, L.; Mai, L. Silicon oxides: A promising family of anode materials for lithium-ion batteries. *Chem. Soc. Rev.* **2019**, *48*, 285–309.

[19] Chae, S.; Choi, S. H.; Kim, N.; Sung, J.; Cho, J. Integration of graphite and silicon anodes for the commercialization of high-energy lithium-ion batteries. *Angew. Chem., Int. Ed.* **2020**, *59*, 110–135.

[20] He, S. G.; Huang, S. M.; Wang, S. F.; Mizota, I.; Liu, X.; Hou, X. H. Considering critical factors of silicon/graphite anode materials for practical high-energy lithium-ion battery applications. *Energy Fuels* **2021**, *35*, 944–964.

[21] Li, X.; Sun, X. H.; Hu, X. D.; Fan, F. R.; Cai, S.; Zheng, C. M.; Stucky, G. D. Review on comprehending and enhancing the initial Coulombic efficiency of anode materials in lithium-ion/sodium-ion batteries. *Nano Energy* **2020**, *77*, 105143.

[22] Li, C.; Liu, B. W.; Jiang, N. Y.; Ding, Y. Elucidating the charge-transfer and Li-ion-migration mechanisms in commercial lithium-ion batteries with advanced electron microscopy. *Nano Res. Energy* **2022**, *1*, e9120031.

[23] Wang, C. Y.; Liu, T.; Yang, X. G.; Ge, S. H.; Stanley, N. V.; Rountree, E. S.; Leng, Y. J.; McCarthy, B. D. Fast charging of energy-dense lithium-ion batteries. *Nature* **2022**, *611*, 485–490.

[24] Lu, G. L.; Liu, F. H.; Chen, X.; Yang, J. F. Cu nanowire wrapped and Cu_3Si anchored Si@Cu quasi core–shell composite microsized particles as anode materials for Li-ion batteries. *J. Alloys Compd.* **2019**, *809*, 151750.

[25] Sun, L.; Liu, Y. X.; Wu, J.; Shao, R.; Jiang, R. Y.; Tie, Z.; Jin, Z. A review on recent advances for boosting initial Coulombic efficiency of silicon anodic lithium ion batteries. *Small* **2022**, *18*, e2102894.

[26] Wu, F.; He, Z. C.; Wang, M. Q.; Huang, Y. D.; Wang, F. Construction of three-dimensional carbon framework-loaded silicon nanoparticles anchored by carbon film for high-performance lithium-ion battery anode materials. *Nano Res.* **2022**, *15*, 6168–6175.

[27] Cao, Z. Y.; Wei, B. Q. A perspective: Carbon nanotube macro-films for energy storage. *Energy Environ. Sci.* **2013**, *6*, 3183–3201.

[28] Yu, Y.; Luo, Y. F.; Wu, H. C.; Jiang, K. L.; Li, Q. Q.; Fan, S. S.; Li, J.; Wang, J. P. Ultrastretchable carbon nanotube composite electrodes for flexible lithium-ion batteries. *Nanoscale* **2018**, *10*, 19972–19978.

[29] Guo, W. L.; Yan, X.; Hou, F.; Wen, L.; Dai, Y. J.; Yang, D. M.; Jiang, X. T.; Liu, J.; Liang, J.; Dou, S. X. Flexible and free-standing SiO_x/CNT composite films for high capacity and durable lithium ion batteries. *Carbon* **2019**, *152*, 888–897.

[30] Yi, Z.; Lin, N.; Zhao, Y. Y.; Wang, W. W.; Qian, Y.; Zhu, Y. C.; Qian, Y. T. A flexible micro/nanostructured Si microsphere cross-linked by highly-elastic carbon nanotubes toward enhanced lithium ion battery anodes. *Energy Storage Mater.* **2019**, *17*, 93–100.

[31] Jiang, H.; Zhou, X.; Liu, G. G.; Zhou, Y. H.; Ye, H. Q.; Liu, Y.; Han, K. Free-standing Si/graphene paper using Si nanoparticles synthesized by acid-etching Al-Si alloy powder for high-stability Li-ion battery anodes. *Electrochim. Acta* **2016**, *188*, 777–784.

[32] Toçoğlu, U.; Hatipoğlu, G.; Alaf, M.; Kayış, F.; Akbulut, H. Electrochemical characterization of silicon/graphene/MWCNT hybrid lithium-ion battery anodes produced via RF magnetron sputtering. *Appl. Surf. Sci.* **2016**, *389*, 507–513.

[33] Chen, C.; Wu, M. Q.; Wang, S. Z.; Yang, J.; Qin, J. G.; Peng, Z.; Feng, T. T.; Gong, F. An *in situ* iodine-doped graphene/silicon composite paper as a highly conductive and self-supporting electrode for lithium-ion batteries. *RSC Adv.* **2017**, *7*, 38639–38646.

[34] Tian, Y.; An, Y. L.; Feng, J. K. Flexible and freestanding silicon/MXene composite papers for high-performance lithium-ion batteries. *ACS Appl. Mater. Interfaces* **2019**, *11*, 10004–10011.

[35] An, Y. L.; Tian, Y.; Zhang, Y. C.; Wei, C. L.; Tan, L. W.; Zhang, C. H.; Cui, N. X.; Xiong, S. L.; Feng, J. K.; Qian, Y. T. Two-dimensional silicon/carbon from commercial alloy and CO_2 for lithium storage and flexible $Ti_3C_2T_x$ MXene-based lithium-metal batteries. *ACS Nano* **2020**, *14*, 17574–17588.

[36] Cao, D.; Ren, M. X.; Xiong, J.; Pan, L. M.; Wang, Y.; Ji, X. Z.; Qiu, T.; Yang, J.; Zhang, C. F. Self-assembly of hierarchical $Ti_3C_2T_x$-CNT/SiNPs resilient films for high performance lithium ion battery electrodes. *Electrochim. Acta* **2020**, *348*, 136211.

[37] Zhang, P.; Zhu, Q. Z.; Guan, Z.; Zhao, Q. R. X.; Sun, N.; Xu, B. A flexible Si@C electrode with excellent stability employing an MXene as a multifunctional binder for lithium-ion batteries. *ChemSusChem* **2020**, *13*, 1621–1628.

[38] An, Y. L.; Tian, Y.; Liu, C. K.; Xiong, S. L.; Feng, J. K.; Qian, Y. T. One-step, vacuum-assisted construction of micrometer-sized nanoporous silicon confined by uniform two-dimensional N-doped carbon toward advanced Li ion and MXene-based Li metal batteries. *ACS Nano* **2022**, *16*, 4560–4577.

[39] Zhang, Z. H.; Ying, H. J.; Huang, P. F.; Zhang, S. L.; Zhang, Z.; Yang, T. T.; Han, W. Q. Porous Si decorated on MXene as free-standing anodes for lithium-ion batteries with enhanced diffusion properties and mechanical stability. *Chem. Eng. J.* **2023**, *451*, 138785.

[40] Guo, X.; Wang, C. D.; Wang, W. J.; Zhou, Q.; Xu, W. J.; Zhang, P. J.; Wei, S. Q.; Cao, Y. Y.; Zhu, K. F.; Liu, Z. F. et al. Vacancy manipulating of molybdenum carbide MXenes to enhance Faraday reaction for high performance lithium-ion batteries. *Nano Res. Energy* **2022**, *1*, e9120026.

[41] Zheng, T. Y.; Jia, Z.; Lin, N.; Langer, T.; Lux, S.; Lund, I.; Gentschev, A. C.; Qiao, J.; Liu, G. Molecular spring enabled high-performance anode for lithium ion batteries. *Polymers* **2017**, *9*, 657.

[42] Yao, D. H.; Yang, Y.; Deng, Y. H.; Wang, C. Y. Flexible polyimides through one-pot synthesis as water-soluble binders for silicon anodes in lithium ion batteries. *J. Power Sources* **2018**, *379*, 26–32.

[43] Tang, R. X.; Ma, L.; Zhang, Y.; Zheng, X.; Shi, Y. J.; Zeng, X. Y.; Wang, X. Y.; Wei, L. M. A flexible and conductive binder with strong adhesion for high performance silicon-based lithium-ion battery anode. *ChemElectroChem* **2020**, *7*, 1992–2000.

[44] Liu, N.; He, W. J.; Liao, H. J.; Li, Z. W.; Jiang, J. M.; Zhang, X. G.; Dou, H. Polydopamine grafted cross-linked polyacrylamide as robust binder for SiO/C anode toward high-stability lithium-ion battery. *J. Mater. Sci.* **2021**, *56*, 6337–6348.

[45] Li, J. W.; Wang, Y.; Xie, X.; Kong, Z.; Tong, Y. H.; Xu, H. Y.; Xu, H.; Jin, H. A novel multi-functional binder based on double dynamic bonds for silicon anode of lithium-ion batteries. *Electrochim. Acta* **2022**, *425*, 140620.

[46] Jin, Y. T.; Kneusels, N. J. H.; Marbella, L. E.; Castillo-Martínez, E.; Magusin, P. C. M. M.; Weatherup, R. S.; Jónsson, E.; Liu, T.; Paul, S.; Grey, C. P. Understanding fluoroethylene carbonate and vinylene carbonate based electrolytes for Si anodes in lithium ion batteries with NMR spectroscopy. *J. Am. Chem. Soc.* **2018**, *140*, 9854–9867.

[47] Tan, L. W.; Sun, Y.; Wei, C. L.; Tao, Y.; Tian, Y.; An, Y. L.; Zhang, Y. C.; Xiong, S. L.; Feng, J. K. Design of robust, lithiophilic, and flexible inorganic-polymer protective layer by separator engineering enables dendrite-free lithium metal batteries with $LiNi_{0.8}Mn_{0.1}Co_{0.1}O_2$ cathode. *Small* **2021**, *17*, e2007717.

[48] Yang, Y. J.; Wu, S. X.; Zhang, Y. P.; Liu, C. B.; Wei, X. J.; Luo, D.; Lin, Z. Towards efficient binders for silicon based lithium-ion battery anodes. *Chem. Eng. J.* **2021**, *406*, 126807.